

## A NEW CONCEPT OF STAINLESS STEEL MEDICAL IMPLANT BASED UPON COMPOSITE NANOSTRUCTURES COATING

L. FLOROIAN<sup>a</sup>, M. FLORESCU<sup>a</sup>, D. MUNTEANU<sup>a</sup>, M. BADEA<sup>a</sup>, G. POPESCU-PELIN<sup>b</sup>, C. RISTOSCU<sup>b\*</sup>, F. SIMA<sup>b</sup>, M.C. CHIFIRIUC<sup>c</sup>, I.N. MIHAILESCU<sup>b</sup>

<sup>a</sup>*Faculty of Electrical Engineering and Computer Science, Transilvania University of Brasov, 29 Eroilor Blvd, 500036 Brasov, Romania*

<sup>b</sup>*Laser-Surface-Plasma Interactions Laboratory, Lasers Department, National Institute for Laser, Plasma and Radiation Physics, 409 Atomistilor street, PO Box MG-36, RO-77125, Magurele, Ilfov, Romania*

<sup>c</sup>*Department of Microbiology, Faculty of Biology, University of Bucharest, 060101 Bucharest, Romania*

A solution to get rid of the inconvenience caused by corrosion of stainless steel implants inside human body is proposed. It consists in coating the stainless steel surface with thin films of bioactive glasses or with bioactive glass - polymer composite nanostructures which may change the implants behavior when inside the physiologic corrosive environment and ensure stability and corrosion resistance to the steel. Potentiodynamic polarization and electrochemical impedance spectroscopy were applied to investigate the corrosion behavior of new structures in simulated body fluids. The corrosion resistance parameters and electrical parameters of the equivalent electric circuits were inferred and verified by fitting the experimental data. The protective coatings proved biocompatible after dedicated assessment experiments, while cells proliferation was boosted.

(Received October 11, 2014; Accepted December 1, 2014)

*Keywords:* Biomedical composites, Corrosion, Laser-assisted transfer, Electrochemical impedance spectroscopy

### 1. Introduction

In last years a great progress has been observed in development of materials with various and specific applications in medicine and biology [1, 2, 3]. Metallic biocompatible materials are commonly used in the reconstruction for operative cardiology and urology, or orthopedic and dental surgery. Many years of clinical experience and assessment of the organism's reaction to metallic biomaterial implants stay at the basis of quantitative or qualitative modifications of their chemical and phase compositions. There exists a strong correlation between the corrosion resistance and the biocompatibility [4, 5]. The corrosion resistance of the biomaterial dictates the reactivity of implant surrounded by tissue and organism fluids. The human body can in no case be considered a friendly host for an implanted metal alloys. It exerts an electrolyte behavior with a pH of around 7.4 and has a temperature of 37°C. Although the chloride solutions are among the most aggressive and corrosive to metals, the ionic composition and protein concentration in body fluids complicate even more the nascent understanding of biomedical corrosion. Moreover, the corrosion products infiltrate tissues, a process described as metallosis [6]. Pathomorphological changes, dependent on the type and concentration of elements, occur thus in tissues close to implant. Histopathological changes were observed in the detoxication organs (liver, kidneys or spleen) [6].

Good biocompatibility is observed for metal and alloys with the high anode potential that can be safely employed for implants within a given time span, stipulating additionally for the

---

\*Corresponding author: carmen.ristoscu@inflpr.ro

particular physical and chemical properties of the implant surfaces. This includes titanium and its alloys [4, 7, 8] or cobalt - chromium alloys [1, 9].

Titanium and its alloys have been used in the human implants for many years. Nevertheless, their corrosion due to dissolution of Ti and alloying elements (e.g. V, Zr or Al among others) is still a cause of concern [1, 4, 6]. Many publications have dealt with the corrosion resistance of titanium implants under various conditions [10-13].

Among the metallic materials, stainless steel is quite popular because of its relatively low cost, ease of fabrication and reasonable corrosion resistance. Nevertheless, stainless steel is susceptible to a number of localized corrosions, such as crevice, pitting, inter-granular and stress corrosion cracking [14]. Several constraints of stainless steel material during its implantation have been mentioned [15] due to high nickel (Ni) content and to the aggressive biological effects.

Corrosion products include iron, chromium, nickel and molybdenum and because of their effects stainless steel are mostly used just as temporary implants to help bone healing, as well as fixed implants such as artificial joints. Typical temporary applications are plates, medullar nails, screws, pins, sutures and steel threads and networks used in fixing fractures [16]. Although stainless steel is seldom used in developed countries as permanent implants, it is still the most used in emerging countries [17].

With this paper we propose a solution to surpass the inconvenience and risks caused by corrosion of stainless steel implants when in the human body. It is shown that the coating with thin films of bioactive glasses or with bioactive glass-polymer nanostructures may change the implants behavior in a physiologic corrosive environment. The bioactive glasses are biomaterials with a great potential which are capable to interact with living materials and can be used in implantology and bone repair applications [18-20]. In bulk the bioglasses are brittle so that they are used as coatings for metallic implants. We previously reported [21, 22] the synthesis of bioactive glass coatings by pulsed laser deposition (PLD) method and nanostructured bioactive glass-polymer coatings by matrix assisted pulsed laser evaporation (MAPLE) on medical titanium substrates that is mechanically suitable for load-bearing orthopedic and dental implants [23]. The obtained layers are bioresorbable in human fluids and a new apatite layer is synthesized by ions changing with the fluid during the bioglass decomposition. In addition, a good adhesion and proliferation of the human cells to bioactive coatings were evidenced.

In this study, the resistance to corrosion of the stainless steel electrodes coated with bioactive glasses or bioactive glasses-polymer was investigated using electrochemical methods that are widely applied due to their high sensibility [24, 25]. Comparative electrochemical measurements involving corrosion and electrochemical impedance spectroscopy studies were carried out in physiological solutions in order to evidence the corrosion behaviour of the medical stainless steel covered with different bioactive films vs. stainless steel bare electrode. The electrochemical parameters of the involved processes were inferred and electrical parameters of the circuits were verified by fitting the experimental data using equivalent electric circuits.

We carefully assessed the biological behaviour of stainless steel samples covered with bioglass or bioglass-polymer thin films in terms of cytotoxicity and biocompatibility when coated with cell cultures.

## **2. Experimental**

### **2.1. Materials**

A bioglass with the code BG57 belonging to the  $\text{SiO}_2\text{-Na}_2\text{O-K}_2\text{O-CaO-MgO-P}_2\text{O}_5$  system was used in the experiments. BG57 contains 56.5%  $\text{SiO}_2$ , 11%  $\text{Na}_2\text{O}$ , 3%  $\text{K}_2\text{O}$ , 15%  $\text{CaO}$ , 8.5%  $\text{MgO}$ , 6%  $\text{P}_2\text{O}_5$  in wt.% and was chosen because of its  $\text{SiO}_2$  content slightly below the threshold value of 60% corresponding to significant changes in bioactivity and degradability.

As deposition substrates, medical grade stainless steel 316L, with the code OL, containing 64.26% Fe, 18.51% Cr, 12% Ni, 2.13% Mo, 1.44% Mn, 0.58% Cu, 0.56% Si, 0.0265% C and other elements in smaller weight percentages is used. These percentages were determined by emission spectroscopy analysis.

Poly(methyl methacrylate) (PMMA) is low cost, easy handling and processing and therefore often used as a lightweight or shatter-resistant alternative to glass [26].

## 2.2. PLD experiment

BG57 powder was pressed with a mould in pellets then sintered at 650°C and used in PLD experiments as targets. Bioglass films were grown by PLD using a pulsed UV KrF\* (248-nm wavelength, with 25-ns pulse duration, 10 Hz frequency repetition rate) excimer laser source and a deposition chamber. The targets were cleaned by a preliminary ablation with 1,000 pulses. A shutter was then interposed between target and substrate, to collect the flux of ablated substance containing impurities.

The (12x12x1) mm<sup>3</sup> OL plates used as collectors were mechanically grounded, polished and chemically etched to reach a roughness in µm range and then carefully cleaned with deionized water in an X-Tra ultrasonic bath.

The laser beam hits the target under an incident angle of 45°. The generated plasma plume expanded normally to target. The ablated material was collected onto the stainless steel substrate placed parallel to the target at a separation distance of 4 cm. In order to avoid drilling and ensure a uniform deposition, the target was rotated with 0.4 Hz frequency and translated along two orthogonal directions.

The laser beam was focused to a 14 mm<sup>2</sup> spot onto the target. The deposition was carried out in a dynamic flux of oxygen. The best PLD regime was found for the next conditions: 13 Pa O<sub>2</sub> pressure, 400°C substrate temperature and 10,000 subsequent laser pulses for the deposition of each film.

## 2.3. MAPLE experiment

Because the use of laser for depositing thin films of polymeric materials is possible by MAPLE technique only [27, 28], for bioglass-polymer composite coating a suspension of 0.5% bioglass in a solution of 3% PMMA in chloroform was prepared and frozen. The frozen composite kept at a constant temperature by cooling with liquid nitrogen served as a target for a thin layer deposition on stainless steel substrates. The selected experimental parameters for depositions were: energy 65 mJ, target-substrate separation distance 4 cm, substrate temperature 30 °C, ambient pressure 2.5 Pa and spot area 36 mm<sup>2</sup>. Each target was irradiated with 2500 laser pulses and the repetition rate was set at 3 Hz.

## 2.4. FTIR analysis

To get information on chemical composition of prepared samples, FTIR analysis was conducted using a Nicolet 380 apparatus equipped with an orbit ATR (diamond crystal), wave number range 7800 – 350 cm<sup>-1</sup>, spectral resolution 0.4 cm<sup>-1</sup>, S/N ratio 20000:1. The spectra were acquired in the absorbance mode. A batch of samples were immersed in SBF at 37° C and investigated after different immersion times. SBF is prepared after Kokubo prescription and has an ionic composition identical to that of plasma blood [29].

## 2.5. Electrochemical studies

Electrochemical studies have been conducted for bare OL and OL substrates coated with BG57 and BG57-PMMA nanocomposite. Anodic and cathodic polarization curves were recorded with a PalmSens potentiostat (Palm Instrument BV) in a three electrodes configuration with an Ag/AgCl reference electrode and a platinum wire as counter electrode. The measurements were performed in SBF. The corrosion extension of program PStace provided the possibility to performed specific types of corrosion measurements and analysis of obtained curves. To obtain reliable results, corrosion measurements for three samples of each type prepared under identical conditions have been conducted. The mean values of corrosion parameters (corrosion potential  $E_{\text{corr}}$  and corrosion rate  $i_{\text{corr}}$ ) along with the computed standard deviation values were calculated.

The plots were registered with 0.002 V/s scan rate and a working potential from -1 V to +2 V vs. Ag/AgCl.

Electrochemical impedance spectroscopy (EIS) analyses were carried out with an Eco Chemie system Autolab PGSTAT 100, three times for each type of sample in the same electrochemical cell that contained fresh SBF. The impedance was measured by frequency response analysis (FRA) technique. An AC potential of 0.01 V amplitude and 10 kHz to 0.1 Hz frequency was applied to the electrochemical cell and the current through the cell was measured. FRA 4.9 software [30] was used to calculate and represent the electrochemical impedance ( $Z_{\text{real}}$  and  $Z_{\text{imag}}$ ) and the phase in Nyquist  $Z_{\text{imag}} = f(Z_{\text{real}})$  or Bode diagrams,  $\text{phase} = f(\text{frequency})$ . Based upon the principles of electrochemical spectroscopy and using the FRA 4.9 software, the equivalent electric circuit best fitting the experimental data with electrical parameters (electrical resistance of the solution, charge transfer resistance and constant phase element) was inferred.

## 2.6. Biological assays

The cell morphology was examined using an inverted, Observer D1 Carl Zeiss microscope.

*Cytotoxicity assay.* The biological compatibility of the obtained material was assessed by cultivating human Wharton's Jelly-derived Mesenchymal Stromal Cells (WJ-MSCs) on their surface. The obtained specimens were sterilized by UV irradiation and placed in 35 mm diameter Petri dishes. In each Petri dish  $3 \times 10^5$  mesenchymal cells were added. The monolayer morphology was evaluated after 24h, by fixing the cells with 70% alcohol and staining the monolayer with 5  $\mu\text{g/mL}$  PI. The stained specimens have been examined by fluorescent microscopy and photographed in UV field according to the protocol in Ref. 31.

*Proliferation assay.* Each specimen was placed in 35 mm diameter Petri dish. In each Petri dish  $3 \times 10^5$  mesenchymal cells were added and incubated for 72 h, to allow them to proliferate on the tested sample. Thereafter, the cells were removed from the device by tripsinisation and analyzed by flow cytometry for the cellular cycle. To this purpose, the cells were washed twice in PBS, and then incubated 15 min, at 37 °C, with RNase A (100  $\mu\text{g/mL}$ ), and 1 h with propidium iodide (100  $\mu\text{g/mL}$ ). After staining of cells with propidium iodide the acquisition was performed using Epics Beckman Coulter flow cytometer. Data were analyzed using FlowJo software and expressed as fractions of cells in the different cell cycle phases.

## 3. Results and discussion

### 3.1. FTIR spectrometry studies

After 1 or 3 days of immersion in SBF, it was noticed for **BG57/OL** samples a higher amplitude of all FTIR peaks in respect with the initial spectrum (Fig. 1a), which is indicative for the formation of a measurable superficial layer where all elements have a larger concentration. This is consistent with other experimental observations on bioglasses [19, 20] and is accompanied by loss of soluble silica in solution.

After one week immersion in SBF, major transformations can be clearly observed on the surface of the coatings. The bioglass peaks at 982  $\text{cm}^{-1}$  and 1008  $\text{cm}^{-1}$  decrease and new maxima appear at 1045  $\text{cm}^{-1}$  (that belongs to asymmetric stretching of P-O bond in  $(\text{PO}_4)^{3-}$ ), at 602  $\text{cm}^{-1}$  (assigned to the vibrational mode of OH) and at 813  $\text{cm}^{-1}$  (corresponding to  $(\text{CO}_3)^{2-}$  group). They belong to a hydroxyl carbonate apatite (HCA) phase [32]. After 7 days of immersion in SBF the spectrum points to a diminishing of silica content and the start of a new HCA layer growth.

In spectra recorded after 14 days of immersion, one can see HCA peaks only, while all bioglass peaks vanished. This suggests either the dissolution of the bioglass and/or the presence on surface of a freshly grown layer similar to carbonated hydroxyapatite  $(\text{Ca}_{10}(\text{PO}_4)_3(\text{CO}_3)_3(\text{OH})_2)$  which is the predominant mineral component in vertebrate bones. The growth of this layer demonstrates the ability of the material to firmly bind to tissue via a bioactive fixation by a chemical bond at the bone-implant interface.

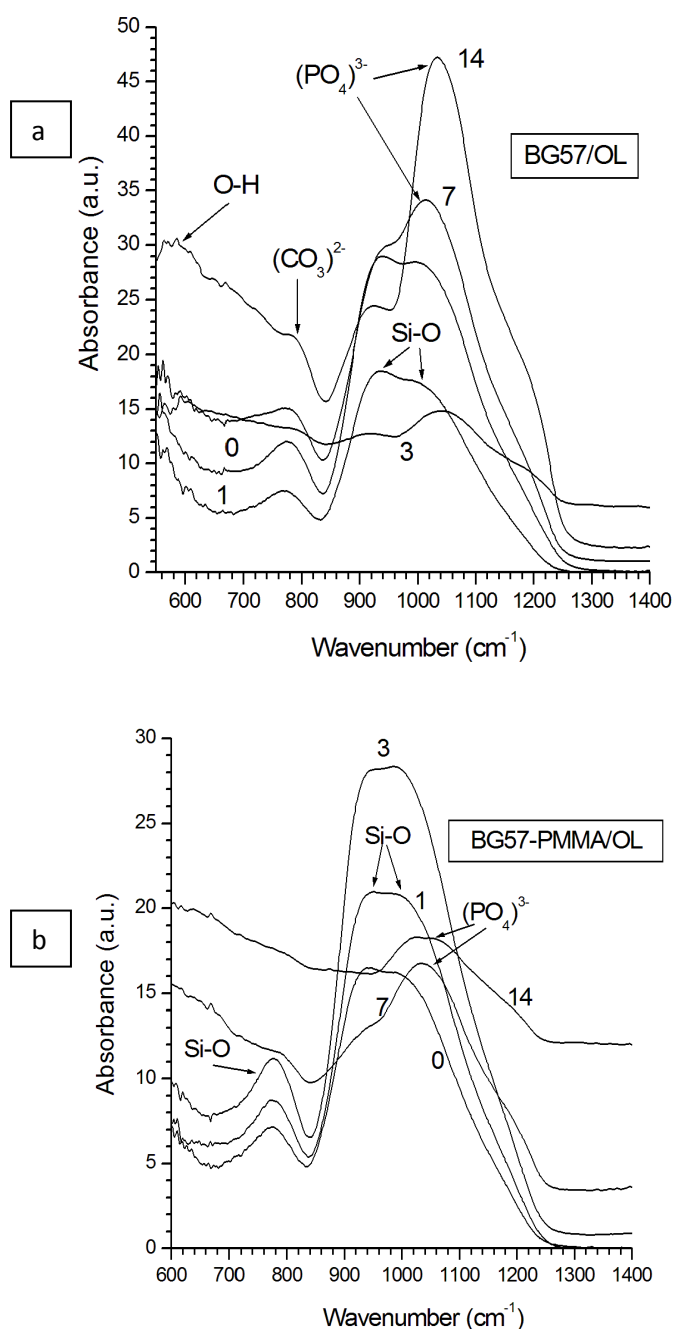


Fig. 1. FTIR spectra of BG61/316L (a) and PMMA-BG61/316L (b) after different time of immersion in SBF

The surface of **PMMA-BG57/OL** samples exhibit similar transformations as BG57/OL ones but in a slower process (Fig. 1b).

### 3.2. Corrosion investigations

The dependence of the corrosion behavior on electrode immersion time for different type of electrodes was studied. The Tafel diagrams for all electrodes are shown in Fig. 2 and the corrosion parameters are collected in Table I. All current densities were normalized to the surface area. Low values of standard deviation (0.01-0.05)  $\mu\text{A}/\text{cm}^2$  have been obtained, which means the results are quite reproducible.

In case of OL, the work electrode initial value of  $i_{\text{corr}} = 13.41 \mu\text{A}/\text{cm}^2$  is one order of magnitude higher than for Ti ( $i_{\text{corr Ti}} = 1.32 \mu\text{A}/\text{cm}^2$  [25]). It follows that, OL corrosion resistance is much smaller. In the same time, OL corrosion potential  $E_{\text{corr}} = -507.22 \text{ mV}/\text{Ag}/\text{AgCl}$  is inferior to Ti ( $E_{\text{corr Ti}} = -357 \text{ mV}/\text{Ag}/\text{AgCl}$  [23]) and decreases with immersion time down to  $-695.19 \text{ mV}/\text{Ag}/\text{AgCl}$ . The corrosion current density increases, reaching  $18.20 \mu\text{A}/\text{cm}^2$ , which suggest that both the passivity and corrosion resistance of OL are inferior to Ti. This is why OL is not preferred for implants manufacturing.

Table I: Corrosion parameters

Time of immersion	0 days		3 days		7 days		14 days	
Corrosion parameters	$E_{\text{corr}}$ (mV vs Ag/AgCl)	$i_{\text{corr}}$ ( $\mu\text{A}/\text{cm}^2$ )	$E_{\text{corr}}$ (mV vs Ag/AgCl)	$i_{\text{corr}}$ ( $\mu\text{A}/\text{cm}^2$ )	$E_{\text{corr}}$ (mV vs Ag/AgCl)	$i_{\text{corr}}$ ( $\mu\text{A}/\text{cm}^2$ )	$E_{\text{corr}}$ (mV vs Ag/AgCl)	$i_{\text{corr}}$ ( $\mu\text{A}/\text{cm}^2$ )
OL	-507.22	13.41	-552.15	11.17	-620.02	14.71	-695.19	18.20
BG57/OL	-342.71	0.72	-235.11	0.18	-221.91	0.15	-216.74	0.10
BG57-PMMA/OL	-269.56	0.08	-160.07	0.09	-132.42	0.09	-121.15	0.06

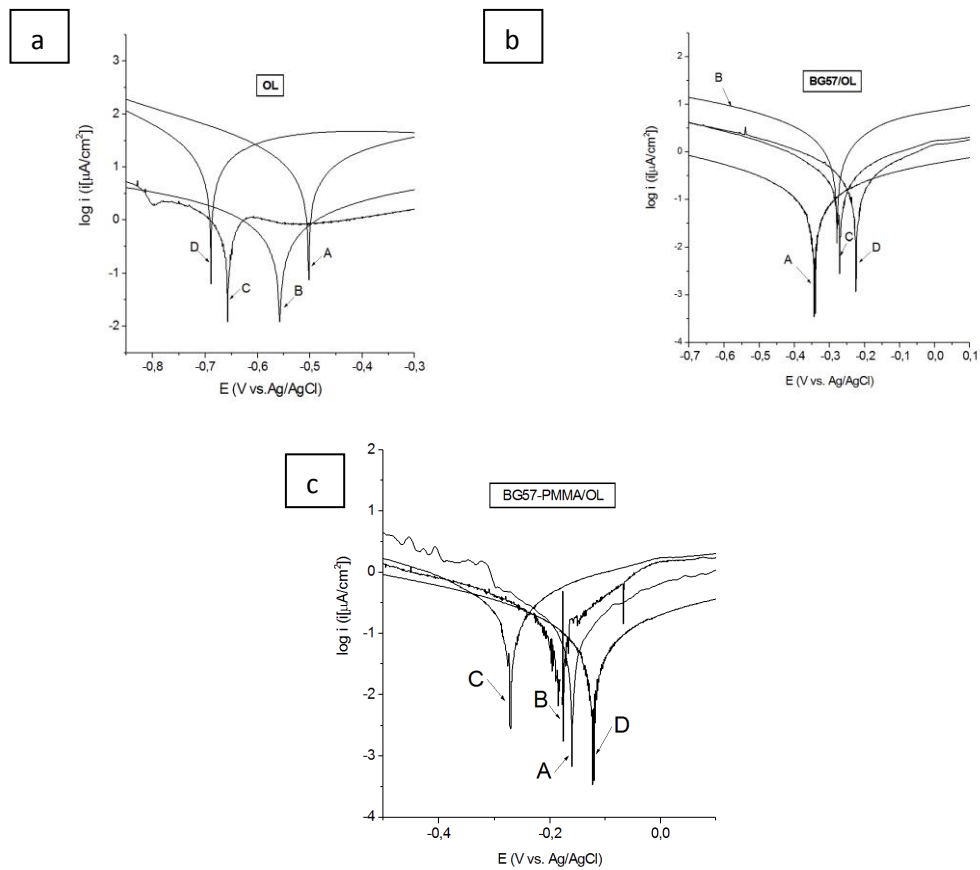


Fig. 2. Tafel curves of bare OL (a), OL covered with BG57 (b) and OL covered with BG57-PMMA (c) after different times of immersion in SBF: A-initial, B-after 3 days, C-after 1 week, D-after 2 weeks.

Large changes appear in OL samples behavior after protection with bioactive glass films. From Fig. 2 and Table I one can see that  $E_{\text{corr}}$  for OL covered with BG57 is higher than for Ti, while corrosion current density is initially half of Ti and significantly decreases in first 7 days of

immersion in SBF. Thus, after 14 days of immersion,  $i_{\text{corr}}$  turns out to be  $0.10 \mu\text{A}/\text{cm}^2$ , much lower than for Ti.

After bioglass-polymer coating of OL, the changes are more important. The corrosion rate drops two orders of magnitude down as compared to bare Ti and continues to decrease slowly with immersion time. These prove that BG-PMMA nanocomposite coatings protect significantly better the OL implants against corrosion.

It results that by coating with BG57 or BG57-PMMA films, the cheap OL implants could get a significantly improved anti-corrosion protection and can successfully replace Ti implants.

### 3.3. Electrochemical impedance spectroscopic (EIS) measurements

To analyze the electrochemical evolution of the coatings under conditions which simulate their biological interactions while inside human body, the samples of OL and OL coated with BG57 and BG57-PMMA thin films were introduced in SBF at  $37^\circ\text{C}$ . The electrochemical impedance spectra after different immersion times (0, 1, 3, 7 or 14 days) were recorded. Measurements were performed in triplicate, with fresh solutions in the same single compartment electrochemical cell.

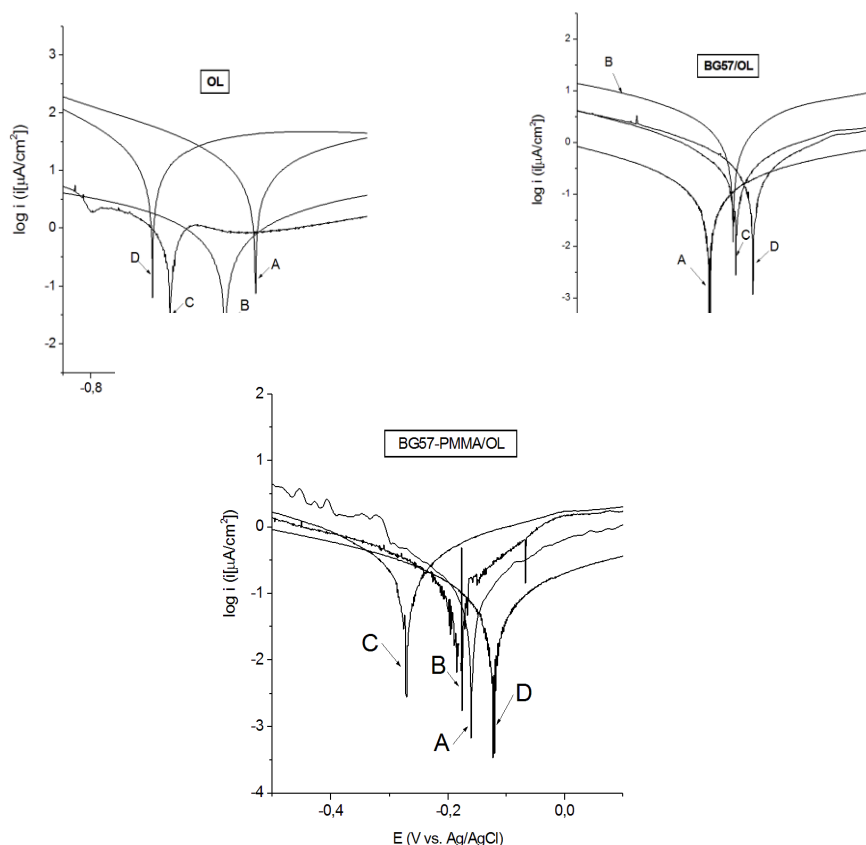


Fig. 3. EIS plots of OL (a), BG57/OL (b) and BG57-PMMA/OL (c) recorded after different times of immersion in SBF

The EIS results for **OL electrode** at the open circuit potential (OCP) configuration presented in Fig. 3a show only one time constant.

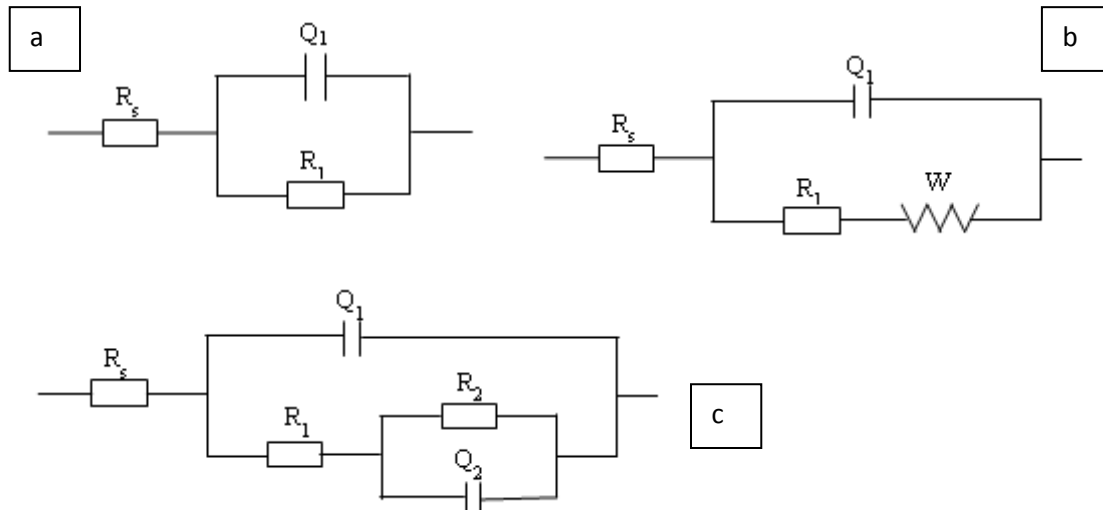


Fig. 4. The equivalent circuits a)  $R_s(Q1R1)$ , b)  $R_s(Q1[R1W])$ , c)  $R_s(Q1[R1(R2Q2)])$  used for fitting the EIS spectra of the samples

The Randles electrical-equivalent circuit resorts to one time constant only (Fig. 4a) used to model the experimental spectra. A good agreement between fitted and experimental data was obtained. Electronic elements in Fig. 4 have the following significance:  $R_s$  is the resistance of the electrolyte between the working and the reference electrode,  $R_1$  is the charge transfer resistance related to the rate of corrosion reaction at the OCP, and it is inversely proportional to the corrosion current, while  $Q$  is the capacitance described by the constant-phase element. As a rule, the use of constant-phase element is mandatory because the relaxation time distribution as a result of inhomogeneities present at the microscopic level at the oxide–electrolyte interface and under the oxide phase. The constant-phase element is a non-ideal capacitor of capacitance  $C$  and roughness factor  $n$ , with  $Q=[C(i\omega)^n]^{-1}$ . The roughness factor  $n$  takes values within  $[0, 1]$  range and it provides information about surface roughness,  $n=1$  corresponding to a perfectly smooth surface and an ideal capacitor. The values of  $R_s$ ,  $R_1$ ,  $C$  and  $n$  obtained from the fits are given in Table I. The maximum phase angle was inferred in each case using Bode plots and is included in the table.

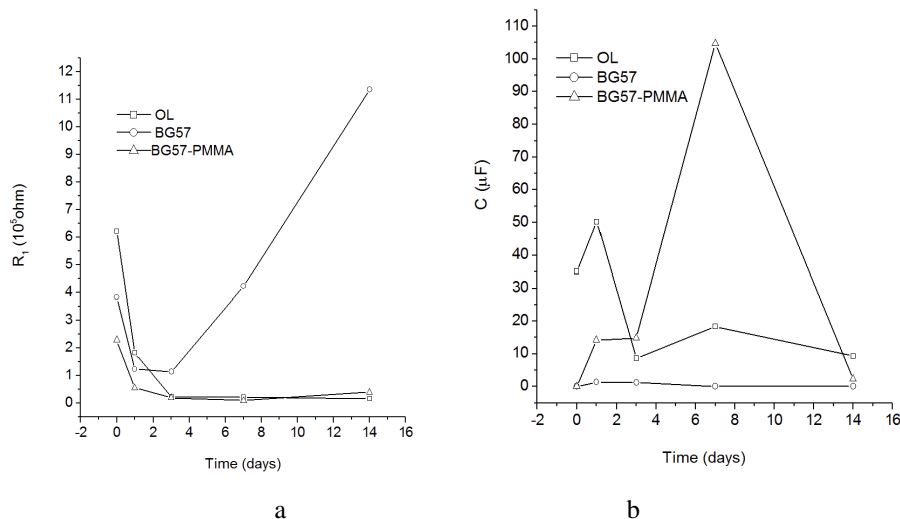


Fig. 5. Charge transfer resistance ( $R_1$ ) (a) and capacitance ( $C$ ) (b) variation with immersion time in SBF

**For OL electrode**, after first day of immersion in SBF, the maximum phase angle decreases from  $67^\circ$  down to  $52.5^\circ$ , charge transfer resistance decreases and capacitance increases (Fig. 5 a, b). All of these point to the intense electrode corrosion inside SBF.

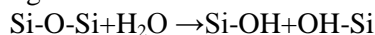
These are inappropriate behaviours for an implant material because can cause the aseptic loosening after implantation, in accordance with Ref. [11]. The undesired effects are removed by covering OL implants with BG57 or BG57-PMMA thin protective layers, when a different behaviour in SBF was observed.

**For OL covered with BG57 layer**, the initial maximum phase angle was  $80^\circ$  suggesting the existence on surface of a highly stable film behaving like pure capacitive impedance. The Nyquist diagram (Fig. 3b) is a beginning of a semicircle with a large radius, whereas the charge transfer resistance has a high value of  $382.35 \text{ k}\Omega$ , and the capacitance has a very small value of  $0.002 \text{ }\mu\text{F}$ . These prove that the thin BG57 layer is a good insulator. The roughness factor is 0.83 because the surface was not perfectly smooth, being mechanically grounded and polished before deposition in order to introduce inhomogeneities to increase the surface active area and bioactivity. The equivalent circuit is the same Randles circuit from Fig. 4a with electrical elements collected in Table II. It is to mention that the parameters from Table II were normalized to the surface area of the each specimen.

**After 1 day** of immersion in SBF at  $37^\circ \text{C}$ , ion exchange between BG and electrolyte results in a great decrease of the charge transfer resistance and the increase of the capacitance, which are reaching values of  $122.91 \text{ k}\Omega$  and  $1.38 \text{ }\mu\text{F}$ , respectively. When a glass reacts with an aqueous solution, both chemical and structural changes occur as a function of time [32]. First, there is a rapid exchange of  $\text{Ca}^{2+}$  and  $\text{Na}^+$  ions from BG with  $\text{H}_3\text{O}^+$  or  $\text{H}^+$  from SBF:



The cation exchange increases the hydroxyl concentration of the solution which attacks the silica glass network:



The Nyquist diagram (Fig. 3c) shows two well defined time constants. The second semicircle is distorted by Warburg impedance represented by a straight line at  $45^\circ$  to the axis suggesting a diffusion process. Correspondingly, in the Bode plot (not shown here) there are two peaks at  $63^\circ$  and  $45^\circ$ . The equivalent circuit becomes now  $R_s(Q_1[R_1W])$  where  $W=0.4 \text{ m}\Omega$  is Warburg impedance (Fig. 4b).

Table II: Electrochemical impedance spectroscopy data of studied samples after various immersion times in SBF at  $37^\circ \text{C}$

Time		0 days	1 day	3 days	7 days	14 days
OL	Equ. circ	$R_s(Q_1R_1)$	$R_s(Q_1R_1)$	$R_s(Q_1R_1)$	$R_s(Q_1R_1)$	$R_s(Q_1R_1)$
	$R_s(\Omega)$	206.12	176.04	201.00	184.36	147.31
	$R_1(\text{k}\Omega)$	621.48	181.19	22.93	20.82	15.01
	$C(\mu\text{F})$	35.12	50.17	8.66	18.38	9.32
	$n$	0.80	0.78	0.56	0.52	0.42
	Max phase angle (grd)	67	63	57	54	52.5
BG57/OL	Equ. circ	$R_s(Q_1R_1)$	$R_s(Q_1[R_1W])$	$R_s(Q_1[R_1(R_2Q_2)])$	$R_s(Q_1R_1)$	$R_s(Q_1R_1)$
	$R_s(\Omega)$	60.91	606.01	91.61	66.14	75.91
	$R_1(\text{k}\Omega)$	382.35	122.91	113.02	421.86	1135.97
	$C_1(\mu\text{F})$	0.002	1.38	1.23	0.001	0.004
	$n_1$	0.83	0.74	0.69	0.81	0.95
	$W(\text{m}\Omega)$		0.40			
	$R_2(\text{k}\Omega)$			299.39		
	$C_2(\mu\text{F})$			3.87		
	$n_2$			0.75		
	Max phase angle (grd)	80	63	61.5	67	81
		45	29			

**After 3 days** of immersion in SBF, the Nyquist diagram shows two well defined time constants and the maximum phase angles become  $61.5^\circ$  and  $29^\circ$ . Two processes, *i.e.* the BG dissolution in SBF and the adsorption of some electrolyte ions on surface, take place simultaneously. The condensation of a  $\text{SiO}_2$ -rich layer on the surface, the migration of  $\text{PO}_4^{3-}$  and  $\text{Ca}^+$  ions through this layer and their adsorption on surface forming a  $\text{CaO-P}_2\text{O}_5$ -rich film are taking place. The BG dissolution leads to the flat surface degradation and the roughness factor gets a much smaller value of 0.69. The equivalent circuit is now  $R_s(Q_1[R_1(R_2Q_2)])$  visible in Fig. 4c. The group  $[Q_1R_1]$  corresponds to an inner layer composed of BG57 degraded coating, while the parallel group  $[R_2Q_2]$  is assigned to an outer layer consisting of  $\text{CaO-P}_2\text{O}_5$ . For the inner layer, the charge transfer resistance is further decreasing and the capacitance increasing, reaching values of 113.02 k $\Omega$  and 1.23  $\mu\text{F}$ , respectively, pointing to the continuous degradation of BG coating. For the outer layer,  $R_2$  and  $C_2$  parameters vary in an opposite way, indicative for the formation of the new  $\text{CaO-P}_2\text{O}_5$  film.

**After 7 days** of immersion in SBF, the amorphous  $\text{CaO-P}_2\text{O}_5$  film crystallizes by incorporation of  $\text{OH}^-$  and  $\text{CO}_3^{2-}$  ions from solution to form the HCA layer. There is a single time constant Nyquist diagram and only the growth of HCA layer takes place. The new apatite layer had the roughness factor of 0.81 and exhibits a charge transfer resistance of 421.86 k $\Omega$  and a double layer capacitance of 0.001  $\mu\text{F}$ . These support the existence on surface of a highly stable film, with characteristics close to pure capacitive impedance that efficiently protects OL against corrosion agents. The EIS fitting generated an equivalent circuit  $R_s(Q_1R_1)$ , as in case of OL coated with BG57 layer after 14 days of immersion in SBF.

**BG57-PMMA coated OL samples** exhibited a similar behaviour with the BG57 coated OL ones, with the difference that the processes take place with lower speed. The initial EIS spectrum evidenced a very stable film with high impedance value, which is supporting a pure capacitive behaviour (Fig. 3c). This compact film well protects the OL substrate against corrosion. The Nyquist diagrams obtained after 3 or 14 days of immersion in SBF at  $37^\circ\text{C}$  show two well distinct time constants suggesting again the simultaneous BG dissolution (K, Na, Si ions migration from electrode to electrolyte) and surface adsorption of  $\text{PO}_4^{3-}$  and  $\text{Ca}^{2+}$  electrolyte ions.

The fitting of EIS spectra has generated a  $R_s(Q_1R_1)$  equivalent circuit before immersion,  $R_s(Q_1[R_1W])$  equivalent circuits for 1 or 3 days of immersion in SBF and  $R_s(Q_1[R_1(R_2Q_2)])$  equivalent circuits for 7 or 14 days, respectively. The parallel group  $(Q_1R_1)$  corresponds to an inner PMMA barrier layer, while the second  $(R_2Q_2)$  parallel group stands for the outer  $\text{CaO-P}_2\text{O}_5$  film. The relevant parameters obtained with the software FRA 4.9 were collected in Table I.  $R_1$  and C values depend on the immersion time as visible from Fig. 5.

Warburg impedance increases with immersion time because the entire amount of glass is dissolved and there are no more species that can diffuse or the new formed layer prevents ions diffusion through. The roughness factor  $n_1$  decreases from 0.91 to 0.67 indicating the surface degradation due to BG dissolution. The roughness factor  $n_2$  of the newly formed  $\text{CaO-P}_2\text{O}_5$  phase increases from 0.42 to 0.62. These points to a porosity reduction and compactness increase of the layer. An important notice is that the compact  $\text{CaO-P}_2\text{O}_5$  layer was much slower forming on the surface of BG57-PMMA samples, after more than 2 weeks of immersion in SBF at  $37^\circ\text{C}$ , compared to BG57 samples when the  $\text{CaO-P}_2\text{O}_5$  film appears after 1 week of immersion only. This delayed formation of the  $\text{CaO-P}_2\text{O}_5$  film could be due to the larger bioactivity of BG57 samples in respect with BG57-PMMA. PMMA addition has reduced the bone ability to bond to BG57. However, as it has been shown before [22], the advantage of using the composite BG57-PMMA derives from the fact that PMMA does not dissolve in SBF but keeps tight to the OL surface. The BG57 bioactivity is preserved after mixing with PMMA and even boosted by the formation of the new  $\text{CaO-P}_2\text{O}_5$  phase on top surface of the coating.

### 3.4. Biological results

The morphology and growth of the WJ-MSCs on the obtained substrata was not affected, in comparison with the control (Fig. 6).

The microscopic results were confirmed by the flow cytometry assay of the cellular cycle, showing no changes in the distribution of the growing phases (Fig. 7).

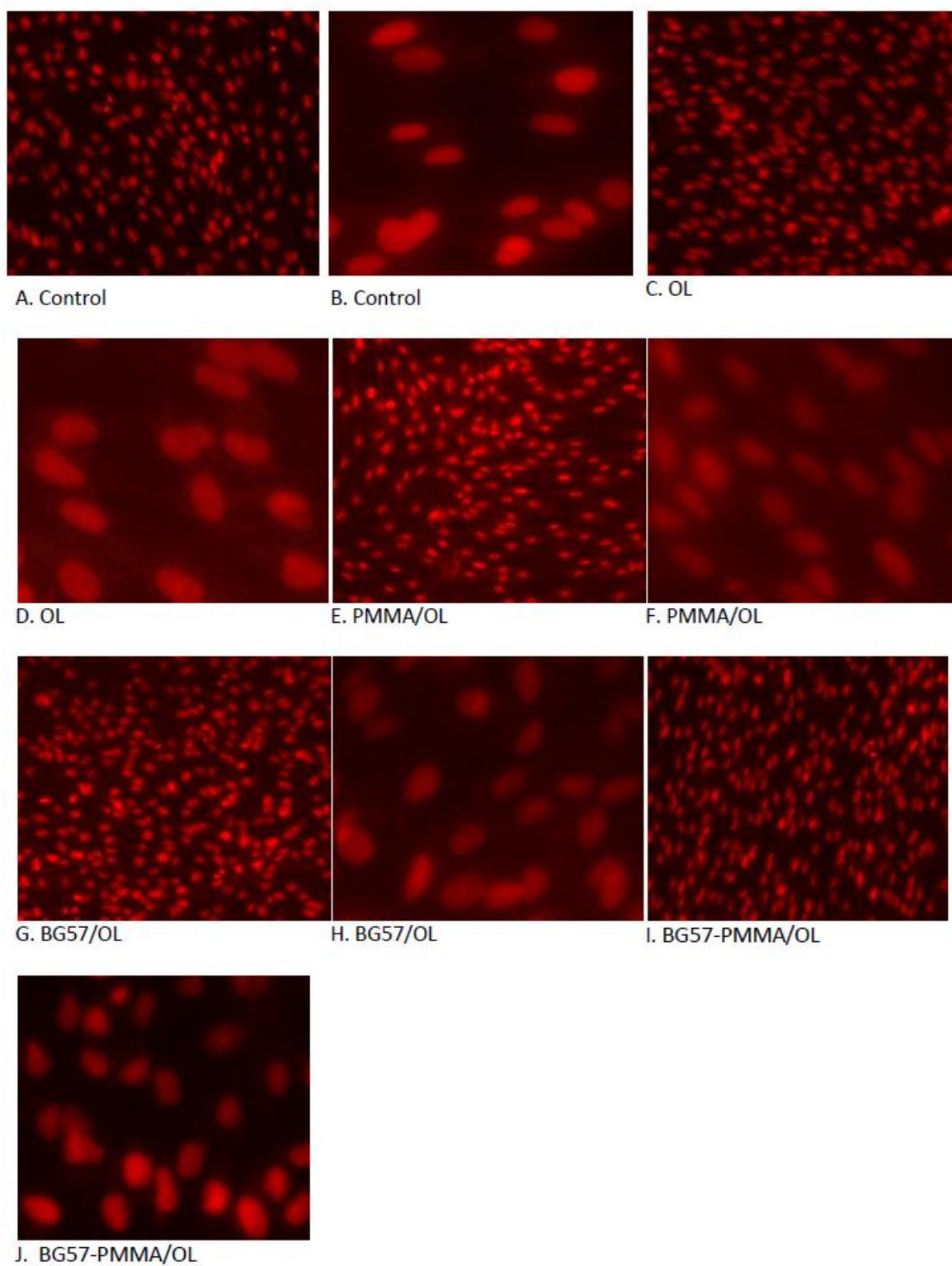


*Fig. 6. Fluorescence microscopy images of WJ-MSCs grown on different substrates. Magnification: 100X (left line), 630X (right line)*

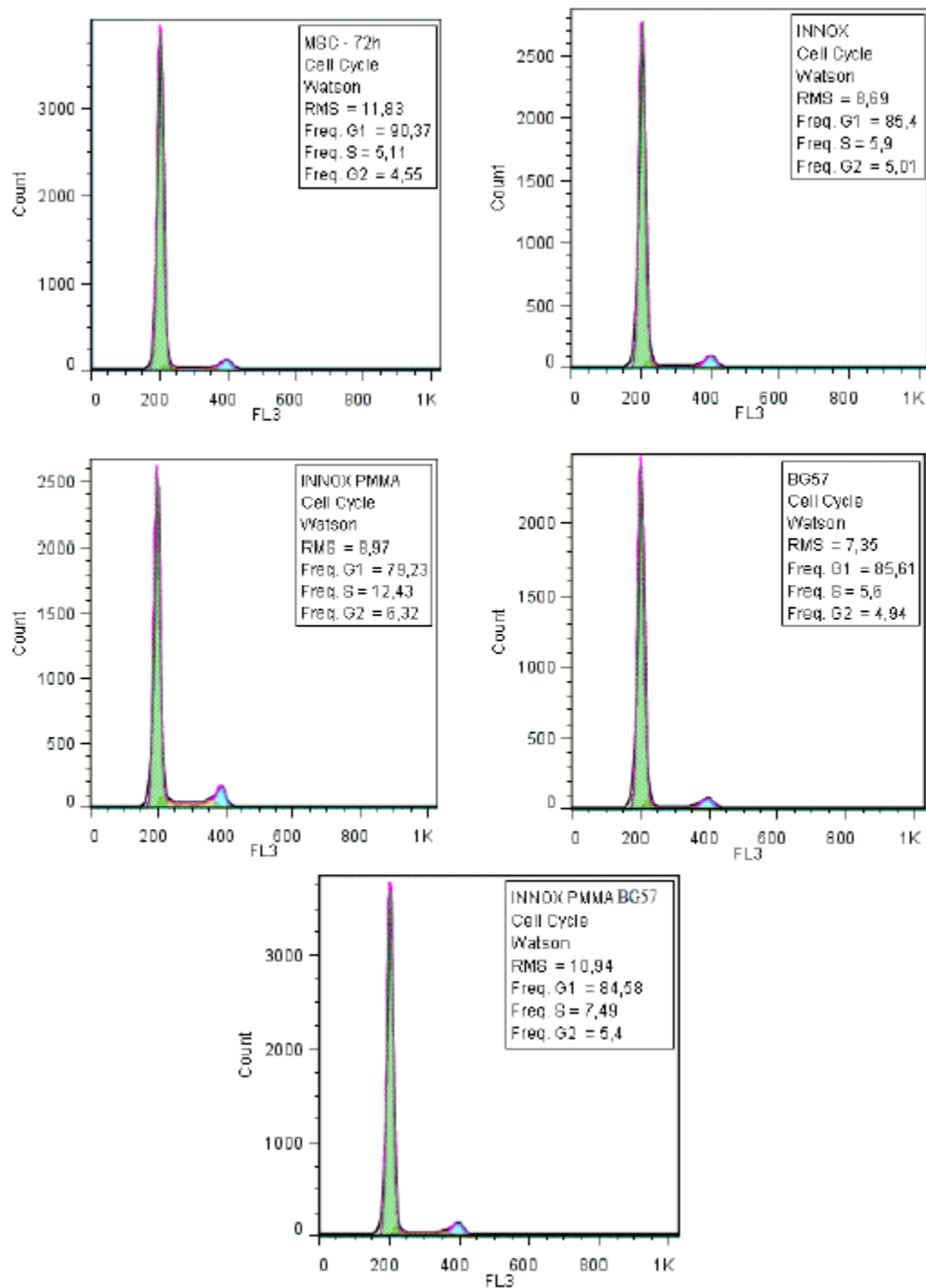


Fig. 7. Curves showing the effects of the obtained specimens on cell cycle progression, assessed by flow cytometry

#### 4. Conclusions

A study on corrosion of bare and coated stainless steel samples in SBF by electrochemical methods is reported. The coatings of BG57 and BG57-PMMA were applied onto OL substrates by PLD and MAPLE, respectively. The growth of WJ-MSCs cells and cytometry studies demonstrated that all deposited layers were entirely biocompatible and fully bioactive. Potentiodynamic polarization investigations evidenced for bare OL an intensive corrosion, but

BG57 and BG57-PMMA coated OL samples presented a substantially higher resistance to corrosion than bare OL. The best shielding was demonstrated in case of BG57-PMMA coating, when practically the corrosion was stopped.

These results are in agreement with FTIR data which demonstrated the formation of a hydroxyl carbonate apatite phase and the growths of a layer similar to carbonated hydroxyapatite which is the predominant mineral component in vertebrate bones.

The EIS data indicate that the films forming on OL substrate after immersion were passive and bi-layered consisting of an inner barrier layer (BG57-PMMA) and an outer porous ( $\text{CaO-P}_2\text{O}_5$ ) layer, which facilitates the osseointegration. It can be concluded that the presence of the BG57 or especially BG57-PMMA coatings on the OL implants surface plays a double role: prevents the release of metal ions into the body fluids and makes the metal surface more bioactive. These results justify the use of these layers for development of advanced, highly stable, low cost stainless steel implants and prostheses not prone to corrosion.

### Acknowledgements

GP-P, CR, FS and INM acknowledge with thanks the financial support of UEFISCDI under the contracts TE 82/2011 and ID304/2011. This paper is also supported by the Sectoral Operational Programme Human Resources Development (SOP HRD), financed from the European Social Fund and by the Romanian Government under the project number POSDRU/159/1.5/S/134378.

### References

- [1] N Eliaz, S Shmueli, I Shur, D Benayahu, D Aronov, G. Rosenman, *Acta Biomater.* **5**, 3178 (2009).
- [2] IN Mihailescu, C Ristoscu, A Bigi, I. Mayer Springer Series in Materials Science; **130**, 235 (2010)
- [3] V Nelea, M Jelinek, IN. Mihailescu, *Biomaterials: new issues and breakthroughs for biomedical applications*. In: Eason R, editor. Pulsed laser deposition of thin films: applications-lead growth of functional materials. New Jersey: Wiley & Sons; 2007. pp. 421.
- [4] YL Zhoua, M Niinomia, T Akahoria, H Fukui, H. Toda, *Mat Sci Eng A-Struct.* **398**, 28 (2005).
- [5] HH Huang, YS Sun, CP Wu, CF Liu, PK Liaw, W. Kai, *Intermetallics*; **30**, 139 (2012).
- [6] T Valimaa, S. Laaksovirta *Biomaterials*; **25**(7-8), 1225 (2004).
- [7] PC Lin, IW Sun, JK Chang, CJ Su, JC. Lin, *Corros Sci.*; **53**, 4318 (2011).
- [8] MB Valcarce, C López, M. Vázquez J. *Electrochem. Soc*; **159**, 244 (2012).
- [9] CV Vidal, AI Muñoz, COA Olsson, S. Mischler, J. *Electrochem. Soc*; **159**, 233 (2012).
- [10] JP Borrajo, J Serra, P Gonzalez, B Leon, FM Munoz, M. Lopez, *J Mater Sci Mater Med.* **18**, 2371 (2007).
- [11] Z Cai, T Shafer, I Watanabe, ME Nunn, T. Okabe, *Biomaterials*; **24**, 213 (2003).
- [12] Y Tsutsumi, S Bartakova, P Prachar, Suyalatu, S Migita, H Doi, N Nomura, T. Hanawa, *J. Electrochem. Soc.*; **159**, 435 (2012).
- [13] BS Ng, I Annergren, AM Soutar, KA Khor, AE. Jarfors, *Biomaterials*; **26**(10), 1087 (2005).
- [14] H Shaikh, N Sivaibharasi, B Sasi, T Anita, R Amirthalingam, BPC Rao, Jayakumar, HS Khatak, B Raj, *Corros Sci.*; **48**(6), 1462 (2006).
- [15] G Rondelli, P Torricelli, M Fini, R Giardino, *Biomaterials*; **26**(7): 739 (2005).
- [16] AWE Hodgson, Y Mueller, D Forster, S. Virtanen, *Electrochim. Acta*; **47**, 1913 (2002).
- [17] J Ballarre, I Manjubala, WH Schreiner, JC Orellano, P Fratzl, S. Cere, *Acta Biomater.* **4**(6) 1601 (2010).
- [18] A Wren, B Akgun, B Adams, A Coughlan, N Mellott, M. Towler, *Biomater Appl.* **27**, 433 (2012).

- [19] M Looney, H O'Shea, D. Boyd, J Biomater Appl.; **27**, 511 (2013).
- [20] C Vitale-Brovarone, G Ciapetti, E Leonardi, N Baldini, O Bretcanu, E Verne, F. Bairo J Biomater Appl; **26**, 465 (2011).
- [21] L Floroian, M Florescu, F Sima, G Popescu-Pelin, C Ristoscu, IN. Mihailescu, Mat. Sci. Eng.C; **32**, 1152 (2012).
- [22] L Floroian, F Sima, M Florescu, M. Badea, AC Popescu, N Serban, IN. Mihailescu J. Electroanal. Chem.; **648**, 111 (2010).
- [23] L Floroian, B Savu, G Stanciu, AC Popescu, F Sima, IN Mihailescu, R Mustata, LE Sima, SM Petrescu, D Tanaskovic, D. Janackovic, Appl Surf Sci.; **255**, 3056 (2008).
- [24] Z Grubač, IŠ Rončević, M Metikoš-Huković, et al. J Electrochem Soc.; **159**, 253 (2012).
- [25] E Rouya, S Cattarin, ML Reed, RG Kelly, G. Zangari, J Electrochem Soc.; **159**, 97 (2012).
- [26] [http://en.wikipedia.org/wiki/Poly\(methyl\\_methacrylate\)](http://en.wikipedia.org/wiki/Poly(methyl_methacrylate))
- [27] R Cristescu, I Stamatina, DE Mihaescu, C Ghica, M Albulescu, IN Mihailescu, DB. Chrisey Thin Solid Films; **453/454**, 262 (2004).
- [28] R Cristescu, DE Mihaescu, G Socol, I Stamatina, IN Mihailescu, DB. Chrisey, Appl Phys A; **79**, 1023 (2004).
- [29] T Kokubo, H Kushitani, S Sakka, T Kitsugi, T. Yamamuro, J. Biomed Mater Res. **24** 721 (1990).
- [30] [http://www.bioeng.nus.edu.sg/people/PI/trau/Lab\\_manuals/Autolab%20manuals/Fra%20manual%204.9.pdf](http://www.bioeng.nus.edu.sg/people/PI/trau/Lab_manuals/Autolab%20manuals/Fra%20manual%204.9.pdf)
- [31] AM Grumezescu, AM Holban, E Andronescu, GD Mogosanu, BS Vasile, MC Chifiriuc, V Lazar, E Andrei, A Constantinescu, H. Maniu, Int. J. Pharm.; **463**(2),146 (2014).
- [32] LL Hench, JR Jones, P Sepulveda, Bioactive materials for tissue engineering scaffolds. In Polak JM, Hench LL and Kemp P, editors. Future Strategies For Tissue And Organ Replacement. London: Imperial College Press, 2002, pp.3-24.